International Journal of Heat and Mass Transfer 52 (2009) 5173–5184

Contents lists available at ScienceDirect

International Journal of Heat and Mass Transfer

journal homepage: www.elsevier.com/locate/ijhmt

Measurement and prediction of pressure drop in a two-phase micro-pin-fin heat sink

Weilin Qu *, Abel Siu-Ho

Department of Mechanical Engineering, University of Hawaii at Manoa, 2540 Dole Street, Holmes Hall 302, Honolulu, HI 96822, USA

ARTICLE INFO

Article history:
Received 8 December 2008
Received in revised form 16 April 2009
Available online 12 June 2009

Keywords:
Micro-pin-fin array
Flow boiling
Pressure drop
Flow instability

ABSTRACT

This study concerns pressure drop in a two-phase heat sink containing an array of staggered square micro-pin-fins having a $200 \times 200\ \mu m^2$ pin cross-section by a 670 μm pin height. Three inlet temperatures of 30, 60 and 90 °C, and six maximum mass velocities for each inlet temperature, ranging from 183 to 420 kg/m^2 s, were tested. Frictional pressure drop in the boiling region is deemed the dominant pressure drop component. The Lockhart–Martinelli correlation for laminar liquid–laminar vapor combination in conjunction with a previous single-phase friction factor correlation can adequately predict the data. Micro-pin-fins offer better flow stability than parallel micro-channels.

1. Introduction

Two-phase micro-pin-fin heat sinks have recently emerged as a promising alternative to two-phase micro-channel heat sinks for thermal management of future generation high-power-density electronic devices [1–3]. Both types of heat sinks utilize micro-size internal structures to enhance heat transfer and capitalize on highly efficient latent heat exchange through liquid flow boiling. They therefore share most common technical merits of two-phase miniature heat sinks, such as very high heat transfer coefficient, small overall heat sink mass and size, small liquid coolant storage and flow rate requirements, and uniform temperature distribution in the stream-wise direction. On the other hand, the two kinds of heat sinks differ from each other in the internal structure configuration. Micro-pin-fin heat sinks incorporate arrays of micro-size pin-fins with diameter ranging from tens to hundreds of micrometers, whereas micro-channel heat sinks use a series of straight plate fins to form multiple parallel micro-channels. Utilization of micro-pin-fin arrays adds an additional advantage of better flow stability to micro-pin-fin heat sinks over their micro-channel counterparts. In fact, appreciable fluctuations in flow pressure and heat sink temperature often occur in two-phase micro-channel heat sinks due to a type of flow instability previously identified as parallel channel instability [4–6]. The type of flow instability is caused by the feedback interaction between parallel micro-channels through the common inlet and outlet manifolds, and is intrinsic to micro-channel configuration itself. The interconnecting nature of flow passages in micro-pin-fin arrays promotes a more uniform pressure field and thus creates a more even two-phase flow distribution, which is expected to yield a more stable flow.

Like their micro-channel counterparts, excessive pressure drop is always a concern for two-phase micro-pin-fin heat sinks due to micro-scale flow passage size and vapor generation. The large pressure drop can lead to considerable pumping power consumption and high operating cost. An accurate pressure drop prediction is therefore of paramount importance to practical implementation of this novel type of heat sink.

As liquid coolant is often supplied to a two-phase miniature heat sink in subcooled state, flow remains liquid single-phase in an upstream region before undergoing liquid-valor phase change in the downstream boiling region where vapor quality rises progressively in the flow direction. Prediction of total heat sink pressure drop therefore requires the knowledge of pressure drops in both single-phase and two-phase (boiling) regions. Several studies have been recently conducted on single-phase pressure drop in micro-pin-fin arrays, which led to revelation of certain unique parametric trends and development of new friction factor correlations [7–14]. Studies on two-phase pressure drop, on the other hand, are rather lacking [15]. Krishnamurthy and Peles studied pressure drop of adiabatic nitrogen-water two-phase flow in an array of staggered circular micro-pin-fins having diameter d of 100 μm, height to diameter ratio H_{fin}/d of 1, longitudinal pitch to diameter ratio S_L/d of 1.5, and transverse pitch to diameter ratio S_T/d of 1.5 [15]. They found that previous two-phase pressure drop correlations developed for conventional size channels, micro-channels, and conventional size tube bundles could not predict their data. The results showed that mass velocity had a significant effect

---

* Corresponding author. Tel.: +1 808 956 6332; fax: +1 808 956 2373.
E-mail address: qu@hawaii.edu (W. Qu).

0017-9310/$ - see front matter © 2009 Elsevier Ltd. All rights reserved.
doi:10.1016/j.ijheatmasstransfer.2009.05.007

Nomenclature

A_c	cross-sectional area of a micro-pin-fin
A_{max}	maximum transverse flow area of micro-pin-fin array
A_{min}	minimum transverse flow area of micro-pin-fin array
A_{p1}, A_{p2}	cross-sectional area of plenums
A_t	platform area of heat sink top surface
$c_{p,f}$	specific heat of liquid water
C	factor in the Lockhart–Martinelli type of correlations
d	diameter of circular pin-fin
d_e	equivalent diameter of a square micro-pin-fin
d_{hch}	equivalent hydraulic diameter of flow passages in micro-pin-fin array
f_{sp}	single-phase friction factor
$f_{sp,f}$	single-phase friction factor based on actual liquid flow rate
f_{tp}	Two-phase friction factor
G	mass velocity
G_{max}	maximum mass velocity
G_{min}	minimum mass velocity
H_{fin}	height of a pin-fin
H_{p2}	height of shallow plenum
i	a stream-wise segment containing one row of micro-pin-fins
K_{c1}, K_{c2}	contraction loss coefficient
K_{e1}, K_{e2}	expansion recovery coefficient
L	length of heat sink top platform area
L_{fin}	length of a micro-pin-fin
$\dot{m}$	total mass flow rate
M	number of data points can be predicted by a model or correlation
MAE	mean absolute error
N_L	total number of micro-pin-fin rows
N_{sub}	number of micro-pin-fin rows in upstream subcooled region
P_{fin}	cross-section perimeter of a micro-pin-fin
P_i	average pressure in the segment i
P_{in}	measured heat sink inlet pressure
P_{out}	heat sink outlet pressure
$P_{sat,0}$	pressure at $z_{sat,0}$
P_W	total electrical power input
ΔP	measured pressure drop across heat sink
ΔP_c	total contraction pressure loss
$\Delta P_{c1}, \Delta P_{c2}$	contraction pressure loss
ΔP_e	total expansion pressure recovery
$\Delta P_{e1}, \Delta P_{e2}$	expansion pressure recovery
ΔP_{sat}	pressure drop in saturated boiling region
$\Delta P_{sat,f}$	frictional pressure drop in saturated boiling region
$\Delta P_{sat,a}$	accelerational pressure drop in saturated boiling region
ΔP_{sub}	pressure drop in subcooled region
q''_{eff}	heat flux based on heat sink top platform area
Q_{loss}	heat loss
S_L	longitudinal pitch
S_T	transverse pitch
Re_{sp}	single-phase Reynolds number
$Re_{sp,f}$	single-phase Reynolds number based on actual liquid flow rate
Re_{tp}	Two-phase Reynolds number
tci	thermocouple ($i = 1-3$)
T_{in}	inlet temperature
T_{out}	outlet temperature
$T_{sat,0}$	saturation temperature at $z_{sat,0}$
v	specific volume
v_{fg}	specific volume difference between saturated vapor and saturated liquid
W	width of heat sink top platform area
W_{fin}	width of a micro-pin-fin
W_{p2}	width of shallow plenum
x_e	thermodynamic equilibrium quality
$x_{e,out}$	thermodynamic equilibrium quality at heat sink outlet
X	Martinelli parameter
X^*	Martinelli parameter in the Dowlati et al. correlation (*SF5*)
$z_{sat,0}$	stream-wise location where thermodynamic equilibrium quality is zero

Greek symbols

α	void fraction
α_h	homogeneous void fraction
ϕ_f	two-phase friction multiplier
μ	viscosity

Subscripts

ave	average
exp	experimental (measured)
f	liquid
g	vapor
i	stream-wise segment
ibd0	upstream boundary of segment *i*
ibdi	downstream boundary of segment *i*
in	inlet
out	outlet
pred	predicted
p1	deep plenum
p2	shallow plenum
tp	two-phase mixture
w	micro-pin-fin base
sat	downstream saturated boiling region
sub	upstream subcooled region

on the two-phase friction multiplier. A new Lockhart–Martinelli type of correlation was proposed, where the C factor was linearly proportional to liquid Reynolds number.

Other relevant studies include those on two-phase pressure drop in conventional size tube bundles several millimeters or larger in diameter [16–21]. Unfortunately, nearly all of these studies adopted aligned configuration while staggered arrangement was favored with micro-pin-fin heat sinks in order to achieve better heat transfer performance [1–3]. The only exception is the work by Dowlati et al. [19], in which pressure drop of adiabatic air-water two-phase flow in two arrays of staggered tube bundles was studied. The tube bundles had diameter d of 19.05 mm and 12.7 mm, longitudinal pitch to diameter ratio S_L/d of 1.3 and 1.75, and transverse pitch to diameter ratio S_T/d of 1.3 and 1.75, respectively [19]. They found that a Lockhart–Martinelli type of correlation with a constant C factor value of 20 could adequately predict their data.

This study aims to further advance our knowledge of the subject matter by investigating pressure drop in a water-cooled two-phase micro-pin-fin heat sink. The heat sink contains an array of staggered square micro-pin-fins with a cross-section of $200 \times 200\ \mu m^2$ and a height of 670 μm. Heat transfer aspect of the heat sink has been reported separately [3]. The objectives of the present study are: (1) to provide new data for pressure drop across a two-phase micro-pin-fin heat sink, (2) to assess the accuracy of existing two-phase pressure drop models and correlations at predicting the present data, (3) to identify the dominant pressure drop component, and (4) to discuss the characteristics of flow instability.

2. Experimental apparatus and procedure

A test module was designed and fabricated for the present experimental study. Fig. 1 shows the construction of the test module that consisted of a 110 copper micro-pin-fin heat sink, a G-7 fiberglass plastic housing, a polycarbonate plastic (Lexan) cover plate, and nine cartridge heaters. The heat sink had a planform (top) area of 3.38 cm (length) by 1.0 cm (width). An array of staggered micro-pin-fins with a $200 \times 200\ \mu\mathrm{m}^2$ cross-section ($W_{fin} \times L_{fin}$) by a 670 μm height (H_{fin}) were milled out of the top surface using a micro-end mill. Square shape was adopted for the pin-fins due to the ease of fabrication. The total number of micro-pin-fin rows in the flow direction was 85. There were nominal 24 pin-fins in every odd row and 23 pin-fins in every even row. A top view of the micro-pin-fin array together with key dimensions is shown in Fig. 2. Uncertainty in micro-pin-fin cross-sectional dimension $W_{fin} \times L_{fin}$ was estimate to be 5 μm, and uncertainty in pin-fin height H_{fin} was 10 μm. Below the heat sink top surface, three type-K thermocouples, indicated in Fig. 1 as *tc1* to *tc3* from upstream to downstream, were inserted along the center plane to measure the stream-wise temperature distribution inside the heat sink. Nine holes were drilled into the bottom surface of the heat sink to accommodate the cartridge heaters that provided heating power during the tests. The cartridge heaters were connected in parallel and powered by a 0–110 *VAC* variac. The total power input P_w was measured using a 0.5% accuracy wattmeter.

Deionized water was employed as the testing liquid. A closed passage for flow across the micro-pin-fin array was formed by inserting the heat sink into the housing and then bolting the cover plate atop. Leak-proof seal was created by applying RTV silicone rubber along the interface between the heat sink and the housing as well as into a shallow groove in the housing around the heat sink top surface. The transparent cover plate facilitated direct visual access to the two-phase flow in the micro-pin-fin array. After the test module was assembled, multiple layers of ceramic fiber were wrapped around the heat sink to reduce heat loss to ambience.

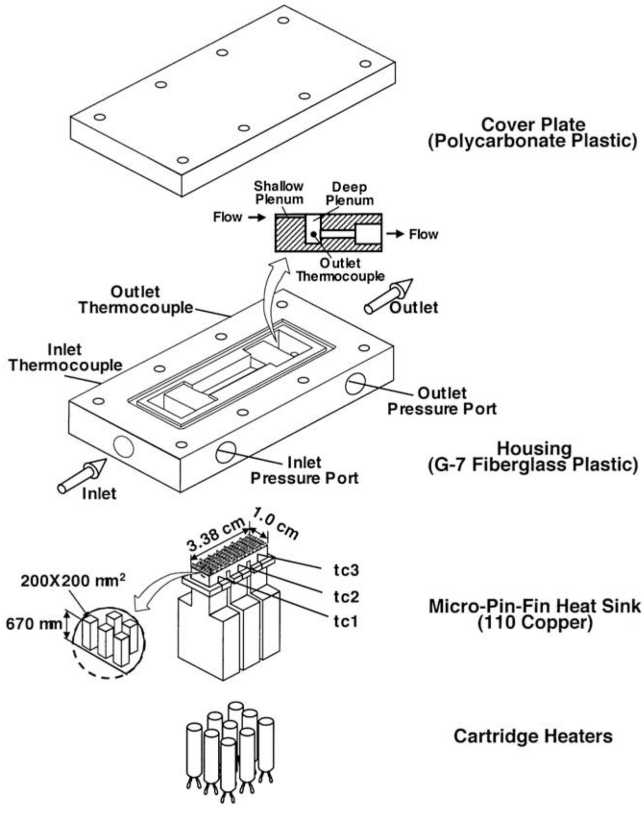

Fig. 1. Test module construction.

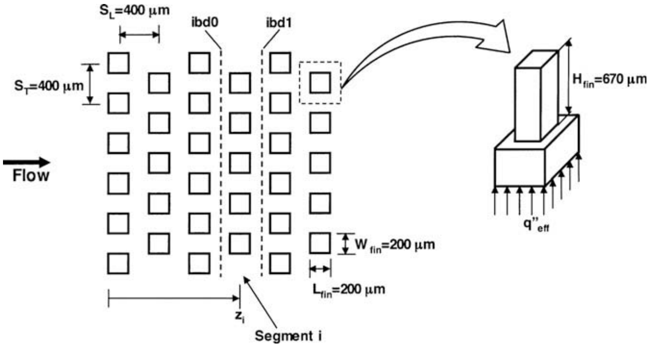

Fig. 2. Top view of micro-pin-fin array and schematic of stream-wise segment.

The housing contained a deep plenum and a shallow plenum both upstream and downstream of the heat sink as shown in Fig. 1. Two thermocouples were located in the deep plenums to measure the inlet and outlet temperatures T_{in} and T_{out}. Errors associated with the thermocouple measurements were smaller than ±0.3 °C. An absolute pressure transducer was connected to the inlet deep plenum via a pressure tap to measure the heat sink inlet pressure P_{in}. A differential pressure transducer was connected to the inlet and outlet deep plenums to measure the pressure drop across the heat sink ΔP. The uncertainty in both P_{in} and ΔP measurements was estimated to be less than 0.25% of the readings.

A flow loop was employed to condition and supply the water to the assembled test module. Fig. 3 shows a schematic of the flow loop. A reservoir stored water and also served as a pressure reference point for the flow loop. In the present study, one atmospheric pressure was maintained inside the reservoir by opening it to ambience. An immersion heater was installed in the reservoir to deaerate water through vigorous boiling. The water was pumped into the flow loop using a gear pump. A compact heat exchanger was used to lower the water temperature to about 19 °C before it entered the pump. After leaving the pump, the water flowed through a filter to prevent solid particles from clogging micro-size flow passages across the micro-pin-fin array. The water then passed through one of two rotameters for mass flow rate $\dot{m}$ measurement. The accuracy of $\dot{m}$ measurement was better than 4% of the readings. Afterwards, the water passed through a second heat exchanger that was connected to a constant temperature bath,

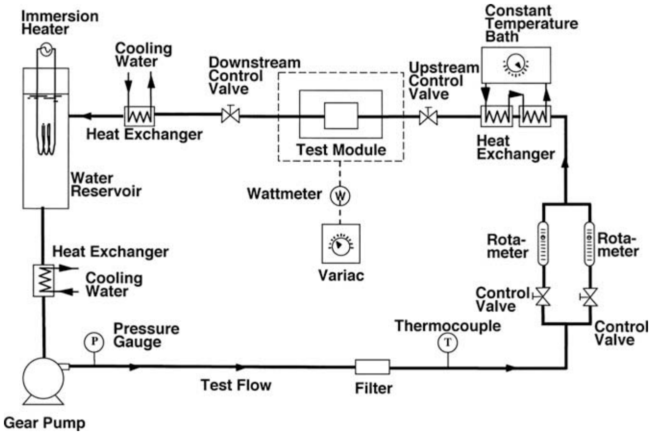

Fig. 3. Schematic of flow loop.

Table 1
Operating conditions.

Inlet temperature, T_{in} (°C)	Mass flow rate, $\dot{m}$ (g/s)	Maximum mass velocity, G_{max} (kg/m^2 s)	Outlet pressure, P_{out} (bar)
30	0.611–1.408	183–420	1.03–1.08
60	0.611–1.398	183–417	1.03–1.08
90	0.611–1.398	183–417	1.03–1.08

where the water was brought to a desired T_{in}. The water then entered the test module. The water exiting the test module flowed through a third heat exchanger to condense vapor before it returned to the reservoir. Two control valves were included in the flow loop for flow control: one located upstream of the test module and the other downstream.

Prior to conducting a test, the water in the reservoir was deaerated for about an hour to force any dissolved gases to escape to ambience. The flow loop components were then adjusted to yield the desired operating conditions. After the flow became stable, P_w was set to a low level where the water flow in the micro-pin-fin array remained single-phase liquid. P_w was then increased in small increments while the desired operating conditions were maintained. At each new P_w level, the heat sink was allowed to reach steady state. Once at steady state, readings from the pressure transducers and thermocouples were recorded at 0.5-s intervals for 3 min using a PC based data acquisition system. Readings from the rotameter and wattmeter were recorded manually. Each test was terminated when the reading from the downstream thermocouple *tc3* inside the heat sink reached about 130 °C to avoid overheating the test module.

Table 1 summarizes the operating conditions in the present study. G_{max} in Table 1 indicates the maximum water mass velocity in the micro-pin-fin array and is defined based on the minimum transverse flow area,

$$G_{max} = \frac{\dot{m}}{A_{min}}, \tag{1}$$

where

$$A_{min} = WH_{fin}\left(1 - \frac{W_{fin}}{S_T}\right). \tag{2}$$

P_{out} in Table 1 represents the heat sink outlet pressure and is evaluated from the measured inlet pressure P_{in} and pressure drop ΔP.

$$P_{out} = P_{in} - \Delta P. \tag{3}$$

Prior to conducting flow boiling tests, a series of water single-phase heat transfer tests were conducted at the same mass flow rates. Results from these single-phase tests were reported in a separate paper [22]. During single-phase tests, heat losses from the test module were evaluated by deducting the measured enthalpy increase of the water flow from the total electrical power input measured by the wattmeter.

$$Q_{loss} = P_W - \dot{m}c_{p,f}(T_{out} - T_{in}). \tag{4}$$

For $T_{in} = 30^{\circ}C$, Q_{loss} ranged from 3% to 15% of P_W [22]. Higher heat losses occurred at lower water mass flow rates. For a given water mass flow rate, it has been observed that Q_{loss} was not sensitive to the electrical power input.

In the present study, the level of input heat flux that was removed from the heat sink is represented by an effective heat flux q''_{eff}, defined based on the top planform area of the heat sink, $A_t = 1.0 \times 3.38$ cm^2.

$$q''_{eff} = \frac{P_W - Q_{loss,ave}}{A_t}, \tag{5}$$

where $Q_{loss,ave}$ represents the average heat loss from the test module at given T_{in} and $\dot{m}$, and is obtained from the previous single-phase heat transfer tests [22].

As the focus of the present study is on pressure drop in the two-phase heat sink, only ΔP data corresponding to a positive outlet thermodynamic equilibrium quality ($x_{e,out} > 0$) are reported in this paper to ensure that the saturated flow boiling condition was established inside the heat sink. The corresponding q''_{eff} ranged from 23.7 to 248.5 W/cm^2.

3. Results and discussion

3.1. Overall pressure drop

Figs. 4–6 present all measured ΔP for T_{in} = 30, 60 and 90 °C, respectively. A total of 400 data points were collected in the present study. Part (a) of each figure plots ΔP versus q''_{eff}, and part (b) versus $x_{e,out}$. For given G_{max} and T_{in}, ΔP increases drastically with increasing q''_{eff} and $x_{e,out}$. The rapid increase in ΔP demonstrates the strong impact of vapor production in the micro-pin-fin array on the total heat sink pressure drop. The results indicate that at moderate to high heat fluxes, which are of special interest to two-phase micro-pin-fin applications, the pressure drop in the

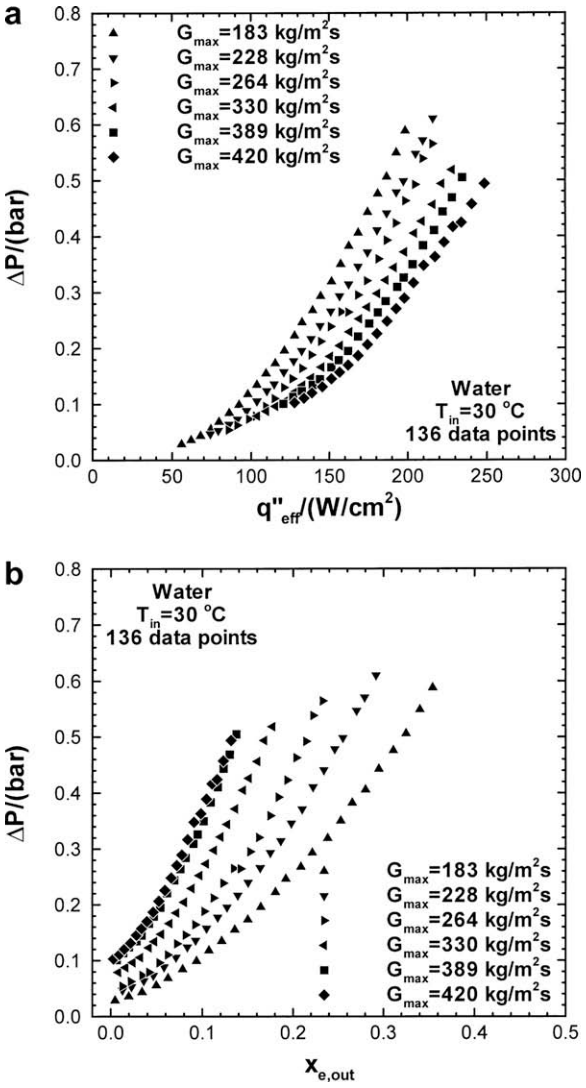

Fig. 4. Measured ΔP for T_{in} = 30 °C as a function of (a) q''_{eff} and (b) $x_{e,out}$.

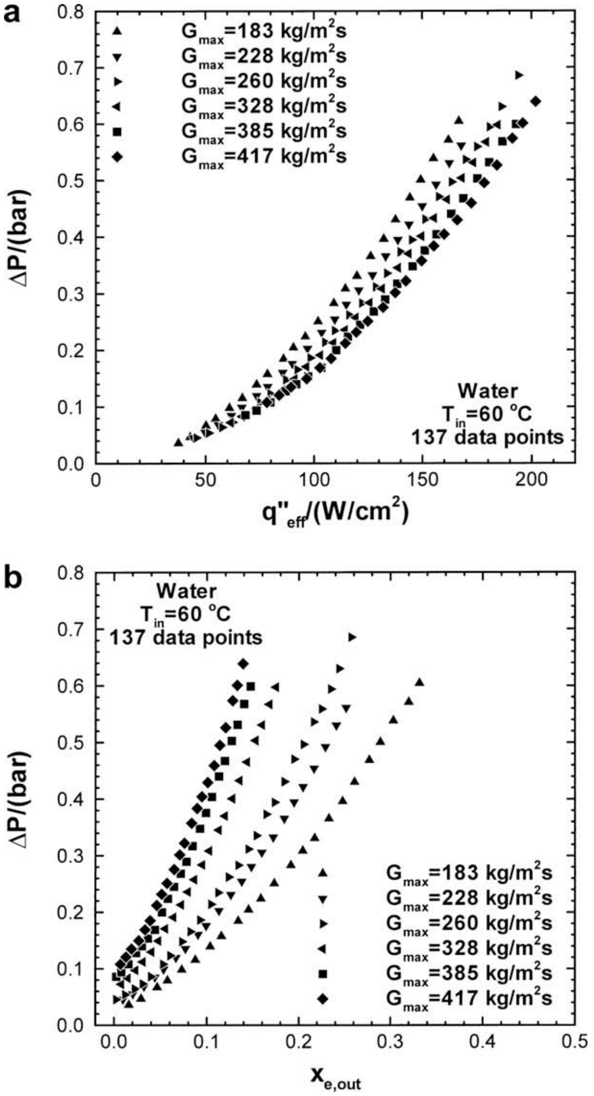

Fig. 5. Measured ΔP for T_{in} = 60 °C as a function of (a) q''_{eff} and (b) $x_{e,out}$.

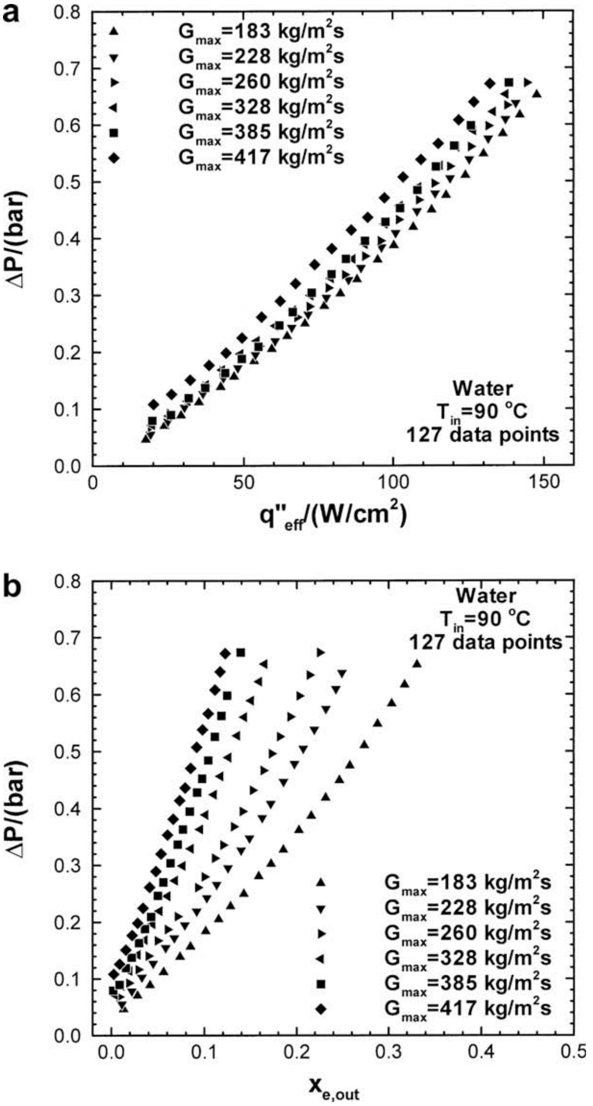

Fig. 6. Measured ΔP for T_{in} = 90 °C as a function of (a) q''_{eff} and (b) $x_{e,out}$.

boiling region could be an order of magnitude higher than that in the single-phase region, and the total pressure drop is overwhelmingly dominated by the former. For fixed $x_{e,out}$ and T_{in}, ΔP increases with increasing G_{max} due to stronger wall friction and body drag effects. The effect of T_{in} on ΔP can be revealed through a close examination of Figs. 4(b), 5(b) and 6(b). For fixed $x_{e,out}$ and G_{max}, ΔP increases with increasing T_{in}, which can be explained by a diminishing effect of the single-phase region as inlet subcooling decreases.

3.2. Determination of pressure drop components

In the present study, the differential pressure transducer was connected to the inlet and outlet deep plenums of the housing. The measured ΔP is therefore the sum of pressure drops across the inlet deep and shallow plenums, micro-pin-fin array, outlet shallow and deep plenums, as well as pressure losses and recoveries associated with the consecutive sections. As the water was supplied to the heat sink in a subcooled state for all the operating conditions as shown in Table 1, the micro-pin-fin array can be divided into two regions along the stream-wise direction based on the water x_e value: an upstream subcooled region ($x_e < 0$) and a downstream saturated boiling region ($x_e \geqslant 0$). The following equation is employed for ΔP prediction, which accounts for all major pressure drop components:

$$\Delta P = \Delta P_{c1} + \Delta P_{c2} + \Delta P_{sub} + \Delta P_{sat} + \Delta P_{e2} + \Delta P_{e1}. \tag{6}$$

Fig. 7 shows a schematic of the flow regions as well as the corresponding pressure drop components.

ΔP_{c1} and ΔP_{c2} in Eq. (6) represent the inlet contraction pressure losses from the deep plenum to the shallow plenum and from the shallow plenum to the micro-pin-fin array, respectively. As thermal conductivity of the G-7 fiberglass plastic housing (~0.29 W/m K) is about three orders of magnitude lower than that of the 110 copper micro-pin-fin heat sink (~380 W/m K), adiabatic flow is assumed in the inlet deep and shallow plenums. ΔP_{c1} and ΔP_{c2} are calculated from [14,23]

$$\Delta P_{c1} = \frac{v_{f,in}}{2}\left(G_{p2,in}^2 - G_{p1,in}^2\right) + \frac{K_{c1}\, v_{f,in}}{2} G_{p2,in}^2, \tag{7}$$

and

$$\Delta P_{c2} = \frac{v_{f,in}}{2}\left(G_{max}^2 - G_{p2,in}^2\right) + \frac{K_{c2}\, v_{f,in}}{2} G_{max}^2, \tag{8}$$

where subscripts $p1$ and $p2$ denote the deep plenum and shallow plenum, respectively. K_{c1} and K_{c2} represent the loss coefficients

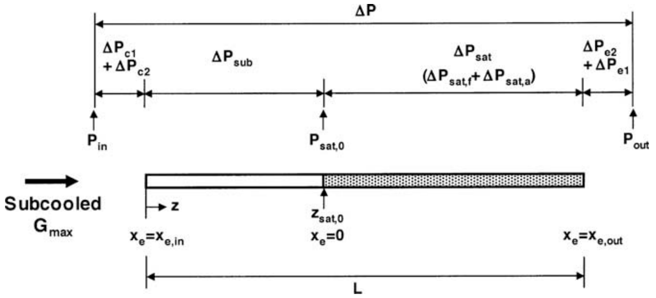

Fig. 7. Schematic of flow regions and pressure drop components.

for the corresponding abrupt contractions and are evaluated from [23]

$$K_{c1}=0.6740+1.2501\left(\frac{H_{p2}}{W_{p2}}\right)+0.3417\left(\frac{H_{p2}}{W_{p2}}\right)^2-0.8358\left(\frac{H_{p2}}{W_{p2}}\right)^3, \tag{9}$$

and

$$K_{c2}=0.6740+1.2501\left(\frac{S_T-W_{fin}}{H_{fin}}\right)+0.3417\left(\frac{S_T-W_{fin}}{H_{fin}}\right)^2-0.8358\left(\frac{S_T-W_{fin}}{H_{fin}}\right)^3. \tag{10}$$

ΔP_{e2} and ΔP_{e1} in Eq. (6) represent the outlet expansion pressure recoveries from the micro-pin-fin array to the shallow plenum and from the shallow plenum to the deep plenum, respectively. Assuming adiabatic two-phase flow in the outlet shallow and deep plenums, ΔP_{e2} and ΔP_{e1} are calculated from [4,14,23]

$$\Delta P_{e2}=\frac{\upsilon_{f,out}+x_{e,out}\upsilon_{fg,out}}{2}\left(G^2_{p2,out}-G^2_{max}\right)+\frac{K_{e2}(\upsilon_{f,out}+x_{e,out}\upsilon_{fg,out})}{2}G^2_{max}, \tag{11}$$

and

$$\Delta P_{e1}=\frac{\upsilon_{f,out}+x_{e,out}\upsilon_{fg,out}}{2}\left(G^2_{p1,out}-G^2_{p2,out}\right)+\frac{K_{e1}(\upsilon_{f,out}+x_{e,out}\upsilon_{fg,out})}{2}G^2_{p2,out}, \tag{12}$$

where K_{e2} and K_{e1} represent the recovery coefficients associated with the corresponding abrupt expansion and are evaluated from [23]

$$K_{e2}=\left(1-\frac{A_{min}}{A_{p2}}\right)^2, \tag{13}$$

and

$$K_{e1}=\left(1-\frac{A_{p2}}{A_{p1}}\right)^2. \tag{14}$$

ΔP_{sub} in Eq. (6) represents the pressure drop across the upstream subcooled region ($x_e < 0$). In addition to liquid single-phase flow, subcooled boiling might also be present in this region. In the present study, it is assumed that the water maintains a single-phase liquid state in the entire subcooled region, and any extra contribution made by the subcooled boiling to ΔP_{sub} is negligible. The assumption is based on the observation that there was no appreciable increase in the measured ΔP prior to the initiation of saturated boiling in the micro-pin-fin array ($x_{e,out}=0$). In a previous study by the present authors [14], the following friction factor correlation was developed based on the adiabatic water single-phase pressure drop data in the present micro-pin-fin array:

$$f_{sp}=20.09Re_{sp}^{-0.547}, \tag{15}$$

where Re_{sp} denotes single-phase Reynolds number and is defined as

$$Re_{sp}=\frac{G_{max}d_e}{\mu_f}. \tag{16}$$

d_e in Eq. (16) represents an equivalent diameter of the square micro-pin-fins,

$$d_e=\frac{4A_c}{P_{fin}}, \tag{17}$$

where A_c is the cross-sectional area of a single micro-pin-fin,

$$A_c=W_{fin}L_{fin}, \tag{18}$$

and P_{fin} is the cross-section perimeter of a single micro-pin-fin,

$$P_{fin}=2(W_{fin}+L_{fin}). \tag{19}$$

Eq. (15) is employed in this study to calculate ΔP_{sub}. In order to better resolve the water property variation in the flow direction, a stream-wise segment based technique is adopted:

$$\Delta P_{sub}=\sum_{i=1}^{N_{sub}}\Delta P_{sub,i}=\sum_{i=1}^{N_{sub}}\left[f_{sp,i}\left(\frac{\mu_{f,i}}{\mu_{w,i}}\right)^{0.58}\frac{\upsilon_{f,i}G^2_{max}}{2}\right], \tag{20}$$

where i indicates a segment in the stream-wise direction that contains a row of micro-pin-fins as well as the surrounding portion of the top and bottom endwalls as shown in Fig. 2, and N_{sub} is the number of micro-pin-fin rows in the subcooled region. All water properties in Eq. (20) except $\mu_{w,i}$ are evaluated based on the average water bulk temperature in the segment i. $\mu_{w,i}$ is evaluated based on the average micro-pin-fin base temperature in the segment i. For brevity, details on how to evaluate these properties are omitted from this paper and can be found in reference [14].

ΔP_{sat} in Eq. (6) represents the pressure drop across the downstream saturated boiling region ($x_e \geqslant 0$). ΔP_{sat} is composed of two components: frictional and accelerational

$$\Delta P_{sat}=\Delta P_{sat,f}+\Delta P_{sat,a}. \tag{21}$$

The frictional component $\Delta P_{sat,f}$ is the result of the wall friction and body drag forces exerted upon the flow by the micro-pin-fin array, and the accelerational component $\Delta P_{sat,a}$ is the result of stream-wise acceleration of the two-phase flow due to phase change. Homogeneous equilibrium model and separated flow model based correlations are two common tools for two-phase pressure drop predictions. In the present study, 10 previous models and correlations that were developed under the framework of homogeneous equilibrium model and separated flow model are selected and applied in conjunction with Eq. (15) to evaluate $\Delta P_{sat,f}$ and $\Delta P_{sat,a}$. The feasibility of using these models and correlations to predict ΔP_{sat} across the micro-pin-fin array is assessed by substituting the results into Eq. (6) and then comparing the predicted ΔP with the measured ΔP. Details of the assessment are presented in the next section.

The knowledge of the stream-wise location $z_{sat,0}$ where x_e reached zero is needed to defined the two flow regions as shown in Fig. 7. In the present study, $z_{sat,0}$ is evaluated from

$$z_{sat,0}=\frac{\dot{m}c_{p,f}(T_{sat,0}-T_{in})}{q''_{eff}W}, \tag{22}$$

where $T_{sat,0}$ is the saturation temperature at $z_{sat,0}$ corresponding to local pressure $P_{sat,0}$. $P_{sat,0}$ is evaluated by deducting $\Delta P_{c1}, \Delta P_{c2}$, and ΔP_{sub} from P_{in},

$$P_{sat,0}=P_{in}-(\Delta P_{c1}+\Delta P_{c2}+\Delta P_{sub}). \tag{23}$$

The two flow regions can therefore be specified by using Eqs. (22), (23), (7), (8), and (20).

3.3. Assessment of previous two-phase pressure drop models and correlations

3.3.1. Homogeneous equilibrium model

Homogeneous equilibrium model treats two-phase mixture as a pseudo-single-phase fluid with average properties that are weighted relative to the vapor and liquid content [24]. Applying homogeneous equilibrium model and adopting the aforementioned segment based technique lead to the following two equations for $\Delta P_{sat,f}$ and $\Delta P_{sat,a}$:

$$\Delta P_{sat,f} = \sum_{i=N_{sub}+1}^{N_L} \Delta P_{sat,f,i} = \sum_{i=N_{sub}+1}^{N_L} \left[f_{tp,i} \frac{v_{f,i} G_{max}^2}{2} \left(1 + x_{e,i} \frac{v_{fg,i}}{v_{f,i}} \right) \right], \quad (24)$$

and

$$\Delta P_{sat,a} = \sum_{i=N_{sub}+1}^{N_L} \Delta P_{sat,a,i} = \sum_{i=N_{sub}+1}^{N_L} G_{min}^2 \left[(v_{f,ibd1} + x_{e,ibd1} v_{fg,ibd1}) - (v_{f,ibd0} + x_{e,ibd0} v_{fg,ibd0}) \right], \quad (25)$$

where N_L is the total number of micro-pin-fin rows in the stream-wise direction ($N_L = 85$), and the subscripts *ibd*0 and *ibd*1 indicate the upstream and downstream boundary of the segment *i*, respectively, as shown in Fig. 2. G_{min} in Eq. (25) represents the water mass velocity at the boundaries of the segment *i* and is evaluated from

$$G_{min} = \frac{\dot{m}}{A_{max}}, \quad (26)$$

where

$$A_{max} = W H_{fin}. \quad (27)$$

f_{tp} in Eq. (24) represents two-phase friction factor. Following Eq. (15), f_{tp} is expressed as

$$f_{tp} = 20.09 Re_{tp}^{-0.547}, \quad (28)$$

where Re_{tp} denotes two-phase Reynolds number,

$$Re_{tp} = \frac{G_{max} d_e}{\mu_{tp}}. \quad (29)$$

μ_{tp} in Eq. (29) represents two-phase viscosity. In the present study, four popular two-phase viscosity models are selected to evaluate μ_{tp} and summarized in Table 2 as models *HE1* to *HE4*.

Calculations of $\Delta P_{sat,f}$ and $\Delta P_{sat,a}$ using Eqs. (24) and (25) commence at $z_{sat,0}$ with local pressure $P_{sat,0}$ and proceed progressively downstream. All the material properties in the segment *i* are determined based on the local pressures that are evaluated from

$$P_{ibd1} = P_{ibd0} - (\Delta P_{sat,f,i} + \Delta P_{sat,a,i}), \quad (30)$$

and

$$P_i = \frac{P_{ibd0} + P_{ibd1}}{2}. \quad (31)$$

Under certain operating conditions, some μ_{tp} models yield a far more rapid decrease in local pressure along the stream-wise direction such that P_i becomes lower than zero within the saturated boiling region. The models are therefore unable to predict $\Delta P_{sat,f}$ and $\Delta P_{sat,a}$ for these operating conditions. As a result, only a portion of the total 400 ΔP data points can have their predicted counterparts when these models are used.

Comparisons between the ΔP data and the predicted values using the four μ_{tp} models are shown in Fig. 8(a)–(d), respectively. The mean absolute error (*MAE*) for each model, defined as

$$MAE = \frac{1}{M} \sum \frac{|\Delta P_{exp} - \Delta P_{pred}|}{\Delta P_{exp}} \times 100\%, \quad (32)$$

where *M* is number of data points that can be predicted by the model, is also presented in the figures. Among the four μ_{tp} models, the best agreement is achieved with the Dukler et al. model (*HE3*) [27], which is able to predict all 400 data points with an overall *MAE* value of 25.3%. The Beattie and Whalley model (*HE4*) [28] is able to predict 386 data points with an overall *MAE* value of 61.6%. The McAdams et al. model (*HE1*) [25] and the Cicchitti et al. model (*HE2*) [26] are able to predict only a small portion of the data points. They overpredict the data by a large margin. The two models that show better agreement with the data (*HE3* and *HE4*) use homogeneous void fraction α_h to weight μ_f and μ_g, while x_e is employed as the weighting factor for μ_{tp} in the models that overpredict the data by a large margin (*HE1* and *HE2*). The observed trend can be attributed to the fact that *HE1* and *HE2* yield substantially higher μ_{tp} values than *HE3* and *HE4* for the conditions tested in this study.

3.3.2. Separated flow model based correlations

The separated flow model based Lockhart–Martinelli type of correlations have been previously used to predict two-phase pressure drop in conventional size [19,29,30] as well as micro-size geometries [4,15,31]. Applying the Lockhart–Martinelli type of correlations to evaluate $\Delta P_{sat,f}$ and $\Delta P_{sat,a}$ leads to the following two equations:

$$\Delta P_{sat,f} = \sum_{i=N_{sub}+1}^{N_L} \Delta P_{sat,f,i} = \sum_{i=N_{sub}+1}^{N_L} \left[f_{sp,f,i} \frac{v_{f,i} G_{max}^2 (1 - x_{e,i})^2}{2} \phi_{f,i}^2 \right], \quad (33)$$

and

$$\Delta P_{sat,a} = \sum_{i=N_{sub}+1}^{N_L} \Delta P_{sat,a,i} = \sum_{i=N_{sub}+1}^{N_L} G_{min}^2 \left\{ \begin{array}{l} \left[\frac{x_{e,ibd1}^2 v_{g,ibd1}}{\alpha_{ibd1}} + \frac{(1-x_{e,ibd1})^2 v_{f,ibd1}}{1-\alpha_{ibd1}} \right] \\ - \left[\frac{x_{e,ibd0}^2 v_{g,ibd0}}{\alpha_{ibd0}} + \frac{(1-x_{e,ibd0})^2 v_{f,ibd0}}{1-\alpha_{ibd0}} \right] \end{array} \right\}, \quad (34)$$

where α represents void fraction. $f_{sp,f}$ in Eq. (33) denotes single-phase friction factor based on actual liquid flow rate. Following Eq. (15), $f_{sp,f}$ is evaluated from

$$f_{sp,f} = 20.09 Re_{sp,f}^{-0.547}, \quad (35)$$

where $Re_{sp,f}$ represents single-phase Reynolds number based on actual liquid flow rate,

$$Re_{sp,f} = \frac{G_{max}(1 - x_e) d_e}{\mu_f}. \quad (36)$$

ϕ_f in Eq. (33) represents two-phase friction multiplier,

$$\phi_f^2 = 1 + \frac{C}{X} + \frac{1}{X^2}, \quad (37)$$

Table 2
Two-phase viscosity models.

Model	Reference	Mixture viscosity	*MAE* (number of data points)
HE1	McAdams et al. [25]	$\mu_{tp} = \left(\frac{x_e}{\mu_g} + \frac{1-x_e}{\mu_f} \right)^{-1}$	193.0% (94)
HE2	Cicchitti et al. [26]	$\mu_{tp} = x_e \mu_g + (1 - x_e) \mu_f$	204.3% (69)
HE3	Dukler et al. [27]	$\mu_{tp} = \alpha_h \mu_g + (1 - \alpha_h) \mu_f$, $\alpha_h = \frac{x_e v_g}{x_e v_g + (1-x_e) v_f}$	25.3% (400)
HE4	Beattie and Whalley [28]	$\mu_{tp} = \alpha_h \mu_g + (1 - \alpha_h)(1 + 2.5\alpha_h) \mu_f$	61.6% (386)

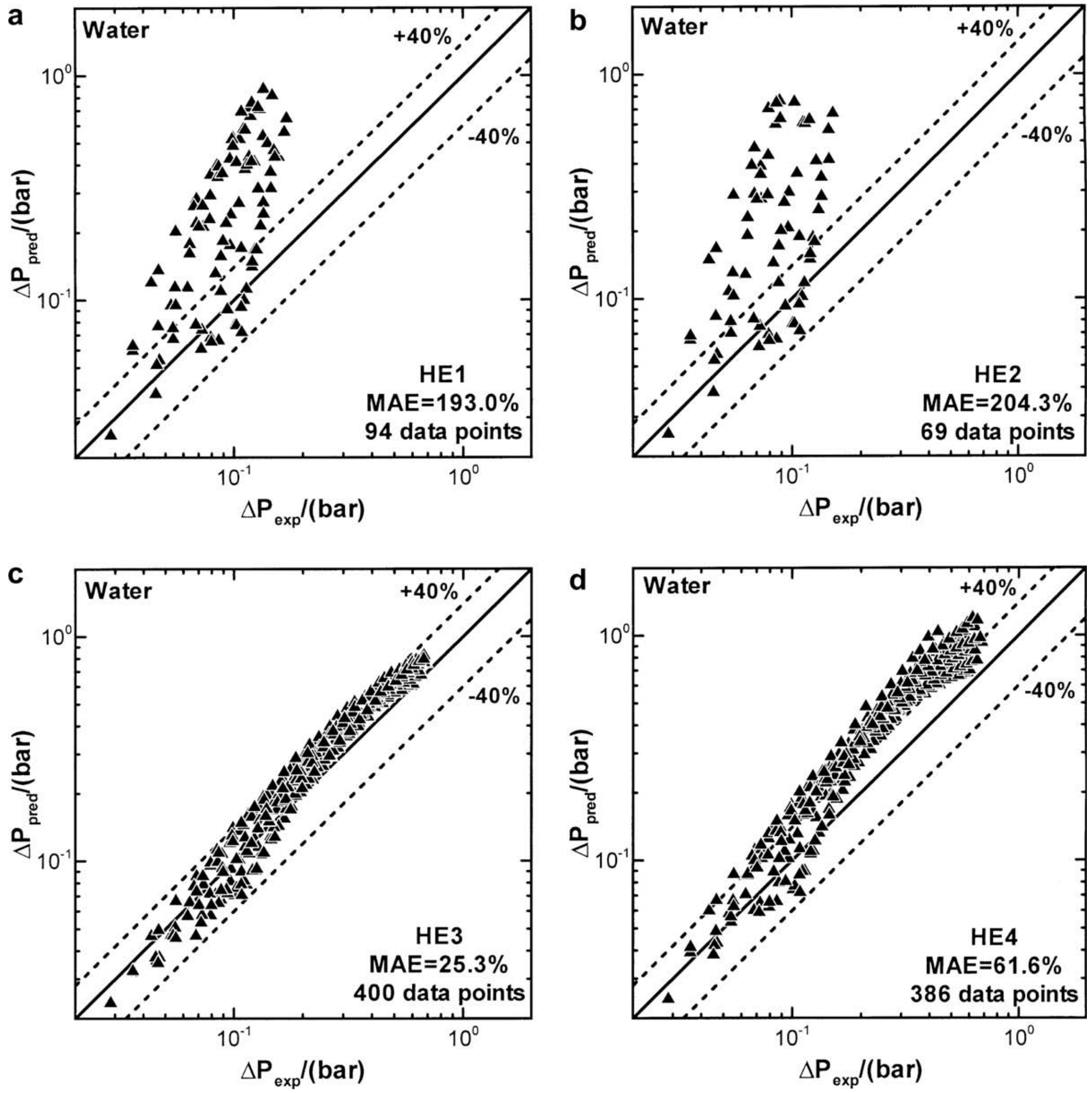

Fig. 8. Comparison of pressure drop data with homogeneous equilibrium model predictions based on two-phase viscosity models by (a) McAdams et al. [25], (b) Cicchitti et al. [26], (c) Dukler et al. [27], and (d) Beattie and Whalley [28].

where X indicates the Martinelli parameter, and C represents an empirical parameter called C factor.

Six previous Lockhart–Martinelli type of correlations are selected, which differ from each other only in the specific relations used for C, X, and α. These correlations are summarized in Table 3 as correlations *SF1* to *SF6*. The Lockhart–Martinelli correlations for laminar liquid–laminar vapor combination (*SF1*) and laminar liquid–turbulent vapor combination (*SF2*) were developed for two-phase flow in conventional size channels [29,30]. The Qu and Mudawar correlation (*SF3*) [4] and the Lee and Garimella correlation (*SF4*) [31] are recent correlations developed based on the pressure drop data of water flow boiling in micro-channels. The Dowlati et al. correlation (*SF5*) [19] and the Krishnamurthy and Peles correlation (*SF6*) [15] were developed for pressure drop of adiabatic gas-water two-phase flow in conventional size tube bundles and micro-pin-fin arrays, respectively.

Fig. 9(a)–(d) compares the ΔP data with the predictions using the four channel flow correlations, *SF1* to *SF4*, respectively. Among the four correlations, the Lockhart–Martinelli correlation for laminar liquid–laminar vapor combination (*SF1*) provides the best agreement with the data, which is able to predict all 400 data points with a *MAE* value of 11.3%. The two micro-channel correlations (*SF3* and *SF4*) show reasonable agreement by predicting all 400 data points and capturing the overall data trend with fairly low scatter. The *MAE* for *SF3* and *SF4* takes a higher value of 36.9% and 17.2%, respectively. The Lockhart–Martinelli correlation for laminar liquid–turbulent vapor combination (*SF2*) can predict 361 data points with an even higher *MAE* value of 95.3%.

Comparisons between the measured ΔP and the predicted values using the two cross flow correlations, *SF5* and *SF6*, are shown in Fig. 10(a) and (b), respectively. The Dowlati et al. correlation (*SF5*) shows large deviation from the data. A possible reason for the discrepancy is that flow was mostly turbulent in conventional tube bundles, while small flow passage size and low flow rate in the micro-pin-fin array yielded dominantly laminar flow. The micro-pin-fin correlation developed by Krishnamurthy and Peles (*SF6*) is able to predict all 400 data points. Despite the moderate *MAE* value of 29.9%, correlation *SF6* seems unable to capture the overall data trend.

Table 3
Lockhart–Martinelli type of correlations.

Correlation	Reference	*C* factor and the Martinelli parameter	Void fraction	*MAE* (number of data points)
SF1	Lockhart and Martinelli (laminar liquid–laminar vapor) [29,30]	$C = 5,\ X = \left(\frac{\mu_f}{\mu_g}\right)^{0.274}\left(\frac{1-x_e}{x_e}\right)^{0.727}\left(\frac{v_f}{v_g}\right)^{0.5}$	$\alpha = 1 - \frac{1}{\sqrt{1+\frac{20}{X}+\frac{1}{X^2}}}$	11.3% (400)
SF2	Lockhart and Martinelli (laminar liquid–turbulent vapor) [29,30]	$C = 12,\ X = \left(\frac{\mu_f}{\mu_g}\right)^{0.274}\left(\frac{1-x_e}{x_e}\right)^{0.727}\left(\frac{v_f}{v_g}\right)^{0.5}$	$\alpha = 1 - \frac{1}{\sqrt{1+\frac{20}{X}+\frac{1}{X^2}}}$	95.3% (361)
SF3	Qu and Mudawar [4]	$C = 21[1-\exp(-319d_{hch})](0.00418G_{max}+0.0613),$ $d_{hch} = \frac{4(S_T-W_{fin})H_{fin}}{2[(S_T-W_{fin})+H_{fin}]},\ X = \left(\frac{\mu_f}{\mu_g}\right)^{0.274}\left(\frac{1-x_e}{x_e}\right)^{0.727}\left(\frac{v_f}{v_g}\right)^{0.5}$	$\alpha = \frac{1}{1+\left(\frac{1-x_e}{x_e}\right)\left(\frac{v_f}{v_g}\right)^{2/3}}$	36.9% (400)
SF4	Lee and Garimella [31]	$C = 2566G_{max}^{0.5466}d_{hch}^{0.8819}[1-\exp(-319d_{hch})],$ $X = \left(\frac{\mu_f}{\mu_g}\right)^{0.274}\left(\frac{1-x_e}{x_e}\right)^{0.727}\left(\frac{v_f}{v_g}\right)^{0.5}$	$\alpha = \frac{1}{1+\left(\frac{1-x_e}{x_e}\right)\left(\frac{v_f}{v_g}\right)^{2/3}}$	17.2% (400)
SF5	Dowlati et al. [19]	$C = 20,\ X^* = \left(\frac{\mu_f}{\mu_g}\right)^{0.1}\left(\frac{1-x_e}{x_e}\right)^{0.9}\left(\frac{v_f}{v_g}\right)^{0.5}$	$\alpha = 1 - \frac{1}{\sqrt{1+\frac{20}{X}+\frac{1}{X^2}}}$	162.8% (152)
SF6	Krishnamurthy and Peles [15]	$C = 0.0358Re_{sp,f},\ X = \left(\frac{\mu_f}{\mu_g}\right)^{0.274}\left(\frac{1-x_e}{x_e}\right)^{0.727}\left(\frac{v_f}{v_g}\right)^{0.5}$	$\alpha = 1 - \frac{1}{\sqrt{1+\frac{20}{X}+\frac{1}{X^2}}}$	29.9% (400)

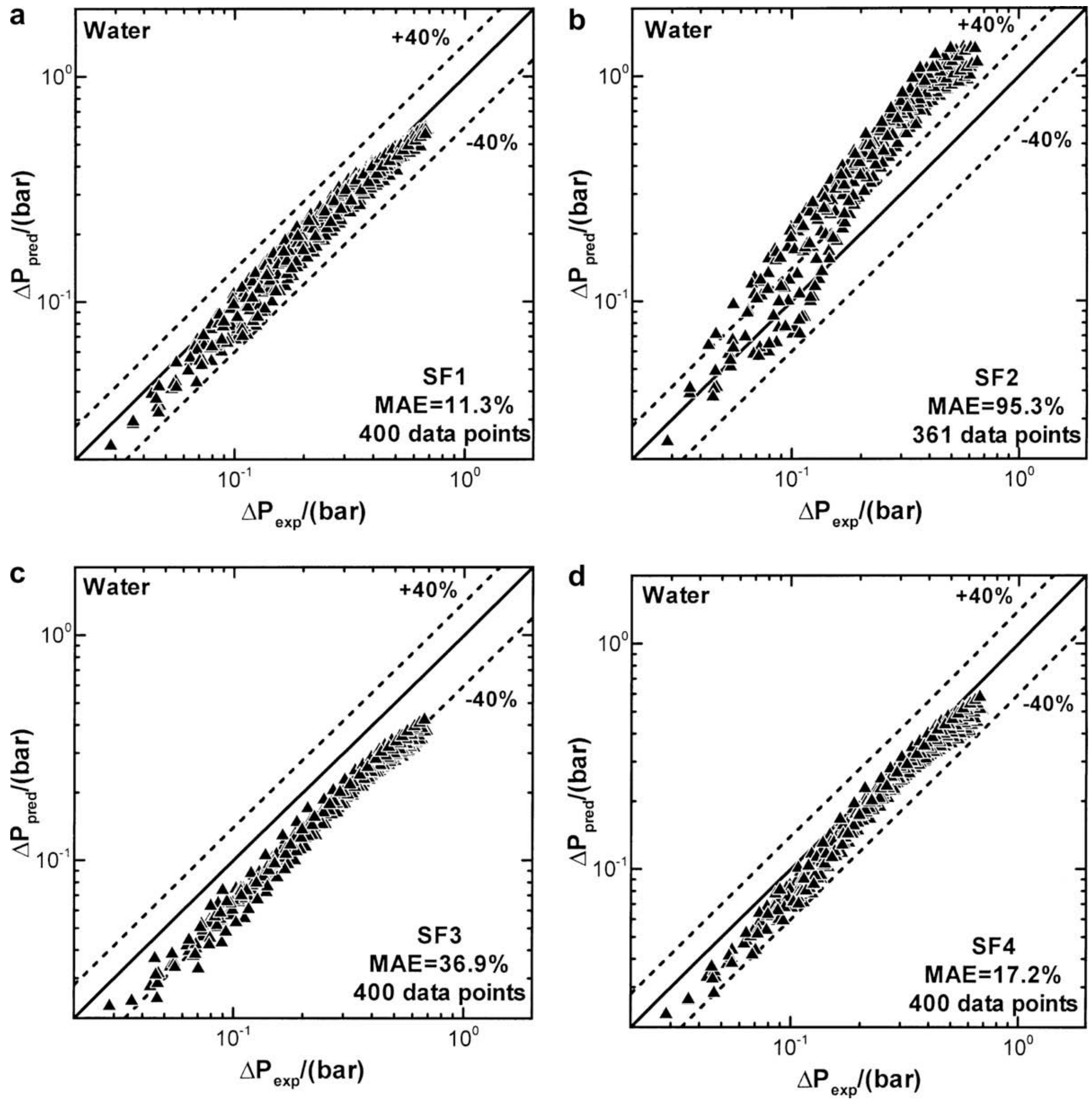

Fig. 9. Comparison of pressure drop data with predictions of Lockhart–Martinelli type of correlations for channel flow by (a) Lockhart–Martinelli (laminar liquid–laminar vapor) [29,30], (b) Lockhart–Martinelli (laminar liquid–turbulent vapor) [29,30], (c) Qu and Mudawar [4], and (d) Lee and Garimella [31].

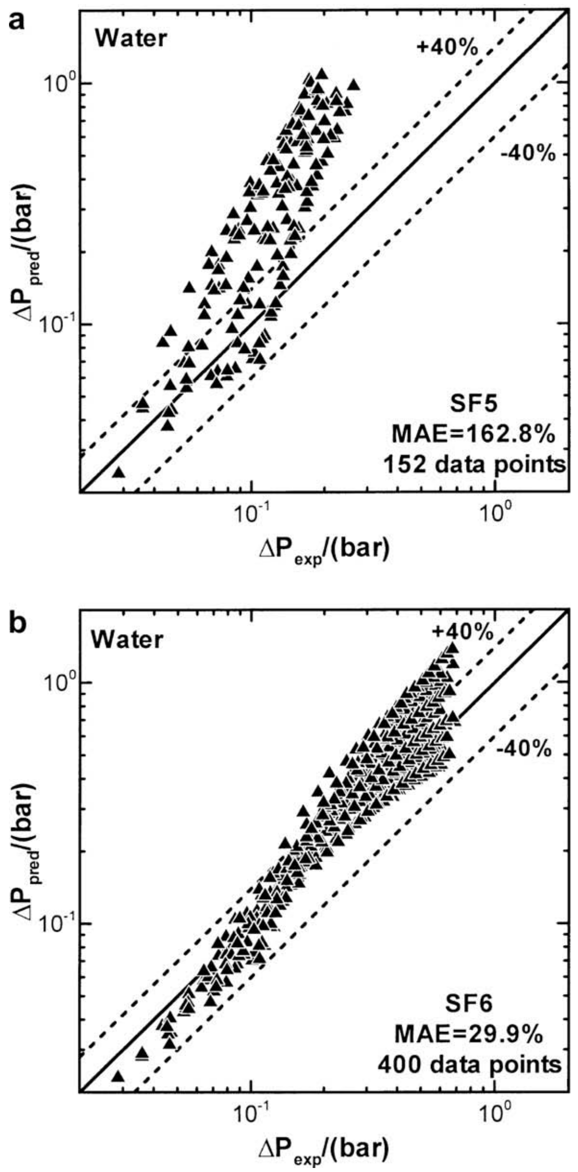

Fig. 10. Comparison of pressure drop data with predictions of Lockhart–Martinelli type of correlations for cross-flow by (a) Dowlati et al. [19], and (b) Krishnamurthy and Peles [15].

In summary, the Lockhart–Martinelli correlation for laminar liquid–laminar vapor combination (*SF1*) in conjunction with Eq. (15) yields the lowest *MAE* value among the 10 previous two-phase pressure drop models and correlations. The two micro-channel correlations (*SF3* and *SF4*) are able to predict the overall data trend, but yield higher *MAE* values. The micro-pin-fin correlation (*SF6*) and homogeneous equilibrium model incorporating the Dukler et al. two-phase viscosity model (*HM3*) yield moderate *MAE* values, but are unable to predict the overall data trend.

3.4. Dominant pressure drop component

From Eq. (6), the predicted ΔP is composed of six pressure drop components. The pressure drop in the saturated boiling region ΔP_{sat} can be further divided into $\Delta P_{sat,f}$ and $\Delta P_{sat,a}$. To reveal the contribution of each component to the total ΔP, the predicted $\Delta P_{sat,f}$, $\Delta P_{sat,a}$, $\Delta P_c(=\Delta P_{c1}+\Delta P_{c2})$, ΔP_{sub}, and $\Delta P_e(=\Delta P_{e2}+\Delta P_{e1})$ are plotted versus q''_{eff} in Fig. 11 for $T_{in} = 60\,^{\circ}\mathrm{C}$ and $G_{max} = 260\ \mathrm{kg/m^2\ s}$ with $\Delta P_{sat,f}$ and $\Delta P_{sat,a}$ evaluated using correlation *SF1*. Also included in Fig. 11 are the measured and predicted ΔP, which show a fairly good agreement. While confirming the previously observation that ΔP_{sat} is the dominant component at moderate to high heat fluxes, Fig. 11 further reveals that between $\Delta P_{sat,f}$ and $\Delta P_{sat,a}$ that comprise ΔP_{sat}, $\Delta P_{sat,a}$ is minuscule except at low heat fluxes. The results indicate that accurate prediction of total pressure drop across a water-cooled two-phase micro-pin-fin heat sink operating at moderate to high heat fluxes is dependent upon the capability of accurately predicting frictional pressure drop in the boiling region.

3.5. Flow instability characteristics

Flow instability in two-phase micro-channel heat sinks have been addressed in previous studies [4–6]. Two types of flow instability were identified. The first type, characterized by severe flow oscillations across the heat sinks, was categorized as pressure drop oscillation. This type of instability was caused by the interaction between the flow boiling in the heat sink and the upstream compressible volume in the flow loop, and could be eliminated by throttling an upstream control valve. The second type, featured mild flow fluctuations between micro-channels, was classified as parallel channel instability. This type of instability was a result of the feedback interaction between parallel micro-channels through the common inlet and outlet manifolds and was intrinsic to the configuration itself.

All the present tests were conducted with the control valve upstream of the test module fully open. The severe flow oscillations that occurred in the two-phase micro-channel heat sinks when the upstream control valve was fully open were never encountered. Instead, two-phase flow fluctuated in the micro-pin-fin array in a fairly mild manner. In the present study, the fluctuation behavior of the inlet pressure P_{in} is employed to indicate the severity of the flow instability.

Reference [4] plotted a temporal record of P_{in} in a two-phase micro-channel heat sink undergoing the parallel channel instability. The figure is reproduced in Fig. 12(a) for comparison purpose. The temporal variation of P_{in} in the present two-phase micro-pin-fin heat sink under a comparable operating condition is plotted in Fig. 12(b). A comparison of the two figures indicates an effective suppression of P_{in} fluctuation by using the micro-pin-fin array.

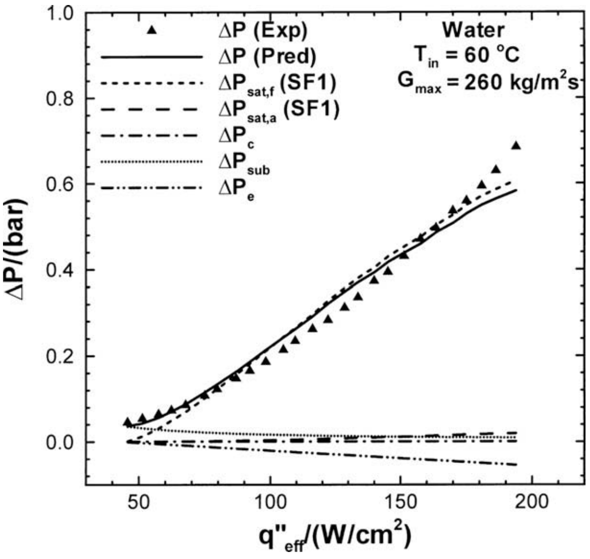

Fig. 11. Contribution of individual pressure drop component to overall heat sink pressure drop for $T_{in} = 60\,^{\circ}\mathrm{C}$ and $G_{max} = 260\ \mathrm{kg/m^2\ s}$.

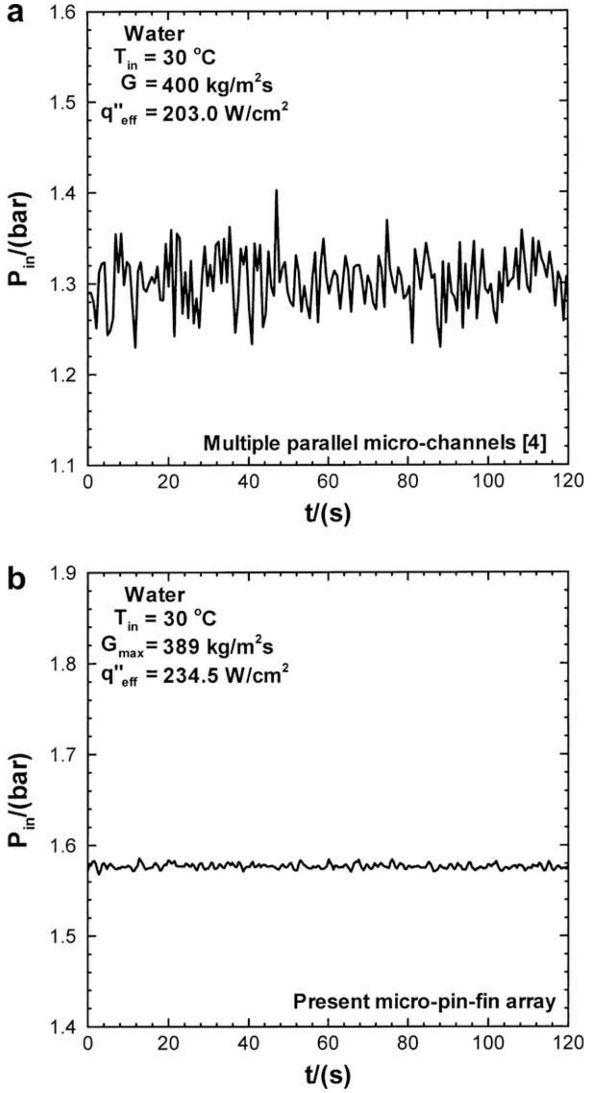

Fig. 12. Temporal records of inlet pressure in (a) the previous two-phase micro-channel heat sink [4] and (b) the present two-phase micro-pin-fin heat sink.

Despite the fact that geometries of the two heat sinks are not identical, i.e., the micro-channel heat sink tested in reference [4] had a planform (top) area of 4.48 cm (length) by 1.0 cm (width) and contained twenty-one 231 μm wide and 712 μm deep rectangular channels, the drastic reduction in the amplitude of P_{in} fluctuation as shown in Fig. 12(a) and (b) nevertheless substantiate the previous claim that micro-pin-fin arrays are able to provide better flow stability than multiple parallel micro-channels.

4. Conclusions

In this study, experiments were conducted to measure pressure drop in a water-cooled two-phase miniature heat sink containing an array of staggered square micro-pin-fins. The experimental study was complemented by assessment of previous two-phase pressure drop models and correlations, identification of the dominant pressure drop component, and discussion of flow instability characteristics. Key findings from the study are as follows:

(1) Vapor production in the micro-pin-fin array has a strong impact on the total heat sink pressure drop. Pressure drop increases drastically once saturated flow boiling commences inside the micro-pin-fin array.
(2) Ten previous two-phase pressure drop models and correlations were examined in predicting pressure drop in the boiling region. The Lockhart–Martinelli correlation for laminar liquid–laminar vapor combination in conjunction with a previous micro-pin-fin single-phase friction factor correlation provides the best agreement with the data. The correlation together with a suitable single-phase friction factor predictive tool is therefore recommended for design of two-phase micro-pin-fin heat sinks.
(3) Frictional pressure drop in the boiling region constitutes the dominant pressure drop component at moderate to high heat fluxes.
(4) Two-phase micro-pin-fin heat sinks are able to provide better flow stability than their micro-channel counterparts. This is because the interconnecting nature of flow passages in micro-pin-fin arrays promotes a more stable two-phase flow.

Acknowledgments

The authors are grateful for the support of the National Science Foundation (Award No. CBET07-30315). The micro-pin-fin heat sink test section was fabricated at the Laser-Assisted Multi-scale Manufacturing Laboratory, University of Wisconsin – Madison. Prof. Frank Pfefferkorn and Dr. Yongho Jeon's assistance in fabricating the heat sink test section was greatly appreciated.

References

[1] A. Koşar, Y. Peles, Boiling heat transfer in a hydrofoil-based micro-pin fin heat sink, Int. J. Heat Mass Transfer 50 (5–6) (2007) 1018–1034.
[2] S. Krishnamurthy, Y. Peles, Flow boiling of water in a circular staggered micro-pin fin heat sink, Int. J. Heat Mass Transfer 51 (5–6) (2008) 1349–1364.
[3] W. Qu, A. Siu-Ho, Experimental study of saturated flow boiling heat transfer in an array of staggered micro-pin-fins, Int. J. Heat Mass Transfer 52 (2009) 1853–1863.
[4] W. Qu, I. Mudawar, Measurement and prediction of pressure drop in two-phase micro-channel heat sinks, Int. J. Heat Mass Transfer 46 (2003) 2737–2753.
[5] W. Qu, I. Mudawar, Transport phenomena in two-phase micro-channel heat sinks, ASME J. Electron. Packag. 126 (2004) 213–224.
[6] W. Qu, I. Mudawar, Measurement and critical heat flux in two-phase micro-channel heat sinks, Int. J. Heat Mass Transfer 47 (2004) 2045–2059.
[7] A. Koşar, C. Mishra, Y. Peles, Laminar flow across a bank of low aspect ratio micro-pin fins, ASME J. Fluids Eng. 127 (3) (2005) 419–430.
[8] Y. Peles, A. Koşar, C. Mishra, C.J. Kuo, B. Schneider, Forced convective heat transfer across a pin fin micro-heat sink, Int. J. Heat Mass Transfer 48 (17) (2005) 3615–3627.
[9] A. Koşar, Y. Peles, Thermal–hydraulic performance of MEMS-based pin fin heat sink, ASME J. Heat Transfer 128 (2) (2006) 121–131.
[10] A. Koşar, Y. Peles, Convective flow of refrigerant (R-123) across a bank of micro-pin fins, Int. J. Heat Mass Transfer 49 (17–18) (2006) 3142–3155.
[11] A. Koşar, C. Kuo, Y. Peles, Hydoroil-based micro-pin fin heat sink, in: Proceeding of IMECE 2006, Paper IMECE2006-13257, ASME, 2006.
[12] R.S. Prasher, J. Dirner, J.Y. Chang, A. Myers, D. Chau, D. He, S. Prstic, Nusselt number and friction factor of staggered arrays of low aspect ratio micro-pin-fins under cross-flow for water as fluid, ASME J. Heat Transfer 129 (2) (2007) 141–153.
[13] A. Siu-Ho, W. Qu, F. Pfefferkorn, Experimental study of pressure drop and heat transfer in a single-phase micro-pin-fin heat sink, ASME J. Electron. Packag. 129 (4) (2007) 479–487.
[14] W. Qu, A. Siu-Ho, Liquid single-phase flow in an array of micro-pin-fins. Part-II. Pressure drop characteristics, ASME J. Heat Transfer 130 (2008) 124501-1–124501-4.
[15] S. Krishnamurthy, Y. Peles, Gas-liquid two-phase flow across a bank of micropillars, Phys. Fluids 19 (4) (2007) 043302-1–043302-14.
[16] K. Ishihara, J.W. Palen, J. Taborek, Critical review of correlations for predicting two-phase flow pressure drop across tube banks, Heat Transfer Eng. 1 (3) (1980) 23–32.
[17] D.S. Schrage, J.-T. Hsu, M.K. Jensen, Two-phase pressure drop in vertical crossflow across a horizontal tube bundle, AIChE J. 34 (1) (1988) 107–115.
[18] R. Dowlati, M. Kawaji, A.M.C. Chan, Pitch-to-diameter effect on two-phase flow across an in-line tube bundle, AIChE J. 36 (5) (1990) 765–772.
[19] R. Dowlati, A.M.C. Chan, M. Kawaji, Hydrodynamics of two-phase flow across horizontal in-line and staggered rod bundles, ASME J. Fluids Eng. 114 (1992) 450–456.

[20] R. Dowlati, M. Kawaji, A.M.C. Chan, Two-phase crossflow and boiling heat transfer in horizontal tube bundles, ASME J. Heat Transfer 118 (1) (1996) 124–131.
[21] G.P. Xu, K.W. Tou, C.P. Tso, Two-phase void fraction and pressure drop in horizontal crossflow across a tube bundle, ASME J. Heat Transfer 120 (1998) 140–145.
[22] W. Qu, A. Siu-Ho, Liquid single-phase flow in an array of micro-pin-fins. Part-I. Heat transfer characteristics, ASME J. Heat Transfer 130 (2008) 122402-1–122402-11.
[23] R.D. Blevins, Applied Fluid Dynamics Handbook, Van Nostrand Reinhold, New York, 1984.
[24] J.G. Collier, J.R. Thome, Convective Boiling and Condensation, third ed., Oxford University Press, Oxford, 1994.
[25] W.H. McAdams, W.K. Woods, L.C. Heroman Jr., Vaporization inside horizontal tubes – II. Benzene–oil mixtures, Trans. ASME 46 (1942) 193–200.
[26] A. Cicchitti, C. Lombardi, M. Silvestri, G. Soldaini, R. Zavattarlli, Two-phase cooling experiments – pressure drop, heat transfer and burnout measurement, Energ. Nucl. 7 (6) (1960) 407–425.
[27] A.E. Dukler, M. Wicks III, R.G. Cleveland, Frictional pressure drop in two-phase flow: A. A comparison of existing correlations for pressure loss and holdup, and B. An approach through similarity analysis, AIChE J. 10 (1964) 38–51.
[28] D.R.H. Beattie, P.B. Whalley, A simple two-phase flow frictional pressure drop calculation method, Int. J. Multiphase Flow 8 (1982) 83–87.
[29] R.W. Lockhart, R.C. Martinelli, Proposed correlation of data for isothermal two-phase, two-component flow in pipes, Chem. Eng. Prog. 45 (1949) 39–48.
[30] D. Chisholm, Two-Phase Flow in Pipelines and Heat Exchangers, Longman, New York, 1983.
[31] P.-S. Lee, S.V. Garimella, Saturated flow boiling heat transfer and pressure drop in silicon microchannel arrays, Int. J. Heat Mass Transfer 51 (3–4) (2008) 789–806.